

# Quasi-amorphous and Hierarchical $\text{Fe}_2\text{O}_3$ Supraparticles: Active $T_1$ -Weighted Magnetic Resonance Imaging *in Vivo* and Renal Clearance

Mingrou Ma, Hui Zhu, Jing Ling, Suqin Gong, Yin Zhang, Yunsheng Xia,\* and Zhiyong Tang



Cite This: *ACS Nano* 2020, 14, 4036–4044



Read Online

ACCESS |



Metrics & More



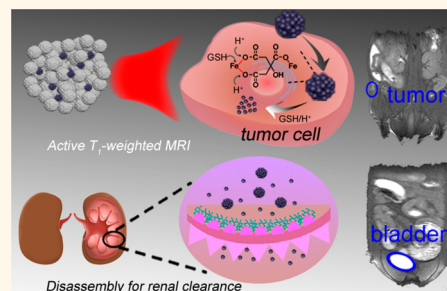
Article Recommendations



Supporting Information

**ABSTRACT:** The exploration of magnetic resonance imaging (MRI) agents possessing excellent performances and high biosafety is of great importance for both fundamental science research and biomedical applications. In this study, we present that monodisperse  $\text{Fe}_2\text{O}_3$  supraparticles (SPs) can act as  $T_1$ -weighted MRI agents, which not only possess a distinct off–on MRI switch in the tumor microenvironment but also are readily excreted from living bodies due to its quasi-amorphous structure and hierarchical topology design. First, the  $\text{Fe}_2\text{O}_3$  SPs have a surface-to-volume ratio obviously smaller than that of their building blocks by means of self-assembly processes, which, on the one hand, causes a rather low  $r_1$  relaxivity ( $0.19 \text{ mM}^{-1} \text{ s}^{-1}$ ) and, on the other hand, can effectively prevent their aggregation after intravenous injection. Second, the  $\text{Fe}_2\text{O}_3$  SPs have a dramatic disassembly/degradation-induced active  $T_1$ -weighted signal readout (more than 6 times the  $r_1$  value enhancement and about 20 times the  $r_2/r_1$  ratio decrease) in the tumor microenvironment, resulting in a high signal-to-noise ratio for imaging performances. Therefore, they possess excellent *in vivo* imaging capacity, even with a tumor size as small as  $5 \text{ mm}^3$ . Third, the disassembled/decomposed behaviors of the  $\text{Fe}_2\text{O}_3$  SPs facilitate their timely clearance/excretion from living bodies. In particular, they exhibit distinct renal clearance behavior without any kidney damage with the right dosage. Fourth, the favorable biodegradability of the as-prepared  $\text{Fe}_2\text{O}_3$  SPs can further relieve the concerns about the unclear biological effects, particularly on nanomaterials, in general.

**KEYWORDS:**  $\text{Fe}_2\text{O}_3$  supraparticles, active  $T_1$ -weighted MRI, quasi-amorphous, renal clearance, biodegradability



Exploration of magnetic resonance imaging (MRI) contrast agents possessing clinical prospects is significant for both fundamental research and practical applications. Until now, two kinds of MRI agents, namely, paramagnetic Gd complexes and superparamagnetic iron oxide nanoparticles (SPIO NPs), have been commercially employed.<sup>1,2</sup> Due to the negative  $T_2$ -weighted signal, SPIO NPs not only possess poor imaging performances but also cause magnetic susceptibility artifacts.<sup>3,4</sup> As a result, some of them have been withdrawn from the market.<sup>5</sup> In contrast, Gd complexes provide a favorable positive  $T_1$ -weighted signal output, which correspondingly dominates the present market. However, Gd deposition in living bodies causes serious nephrogenic systemic fibrosis for patients with decreased renal function.<sup>6</sup> Furthermore, recent studies indicate that Gd deposits have been detected in the brain tissues of patients following administration of Gd(III) contrast agents, even if they have no severe renal dysfunction.<sup>7</sup> As a result, the search for other  $T_1$ -weighted imaging agents has been ongoing.

Similarly,  $\text{Mn}^{2+}$  ions are also good  $T_1$ -weighted imaging agents, but they are also biotoxic.<sup>8,9</sup> Compared with Gd and Mn, Fe has better biosafety. However, it exhibits few advantages for  $T_1$ -weighted output. Recently, based on the rapid development of nanoscience and technology, Fe-based nano- $T_1$ -weighted imaging agents have been well-designed and fabricated. For example, in addition to ultrasmall  $\text{Fe}_2\text{O}_3$  nanocrystals, various nanosubstrates/scaffolds, including  $\text{SiO}_2$  and graphene, have been adopted for the corresponding fabrication.<sup>10,11</sup> Due to the rationally designed extremely large surface-to-volume ratio, these Fe-based nanoimaging agents can interact with  $\text{H}_2\text{O}$

**Received:** October 30, 2019

**Accepted:** March 20, 2020

**Published:** March 20, 2020





molecules and exhibit favorable  $T_1$ -weighted imaging performances even *in vivo*. Despite these substantial achievements, there are a few issues and even problems that are still a concern. First, in addition to uncertain biological effects (graphene and  $\text{SiO}_2$  materials), the biggest issues/problems with nanoentities are their long-term retention, which results in various potential risks/toxicities in living bodies.<sup>12,13</sup> Second, these imaging agents almost exhibit constant signals at any time and place ("always on" mode), leading to poor imaging performances. To address this issue, active MRI design and applications have attracted particular interest in recent years. Based on the trigger/modulation effects of external (light, heat, magnetism, *etc.*) and/or internal (tumor/inflammation micro-environment) means/specific environments, a rationally designed and desired off-on switch of the MRI signal is realized, which can enhance the signal-to-noise ratio compared with the "always on" one. To date, several  $\text{Gd}^{3+}$  ions<sup>14,15</sup> and  $\text{Mn}^{2+}$  ions<sup>16</sup> based on off-on MRI nanoprobes have been reported. However, the use of Fe-based nanoimaging agents for active  $T_1$ -weighted MRI applications, especially *in vivo*, has been limited to several iron-oxide-based nanocluster systems, in which the building blocks are synthesized by high temperature in the organic phase.<sup>17,18</sup> Conceivably, if these problems and limitations can be solved by the development of nanodesign and fabrication strategies, the corresponding applications of nano-MRI imaging agents could be substantially evolved.

To address these issues, we herein present Fe-based  $T_1$ -weighted nano-MRI agents, namely, quasi-amorphous and hierarchical  $\text{Fe}_2\text{O}_3$  supraparticles (SPs), which possess distinctly different and special structure and topology compared to that of their previous counterparts. In addition to the high safety of the components, the quasi-amorphous structure and hierarchical topology endow the SPs with several fascinating properties for MRI applications *in vivo*. First, the  $\text{Fe}_2\text{O}_3$  SPs possess a distinct disassembly/degradation-induced active  $T_1$ -weighted signal readout (more than 6 times the  $r_1$  value enhancement and about 20 times the  $r_2/r_1$  ratio decrease) in the tumor microenvironment (where abundant glutathione and  $\text{H}^+$  decompose  $\text{Fe}_2\text{O}_3$  SPs into small sized  $\text{Fe}_2\text{O}_3$  NPs and even  $\text{Fe}^{3+}$  ions), resulting in a high signal-to-noise ratio for tumor imaging. Therefore, they possess excellent *in vivo* imaging capacity, even with a tumor size as small as 5 mm<sup>3</sup>. Second, the disassembled/decomposed behaviors of the  $\text{Fe}_2\text{O}_3$  SPs facilitate their timely clearance/excretion from living bodies. In particular, they exhibit distinct renal clearance behavior without any kidney damage at the right dosage. Third, the favorable biodegradability of the as-prepared  $\text{Fe}_2\text{O}_3$  SPs can further relieve the concerns about the unclear biological effects, particularly on nanomaterials, in general. Because of the excellent imaging performances, high biosafety, as well as favorable properties (renal clearance and biodegradation), the as-prepared quasi-amorphous and hierarchical  $\text{Fe}_2\text{O}_3$  SPs exhibit great potentials in MRI applications, even for clinical translation research.

## RESULTS AND DISCUSSION

$\text{Fe}_2\text{O}_3$  SPs are fabricated by the proposed *in situ* self-assembly strategy, which is achieved using urea for dynamic pH modulation. The gradual decomposition of urea can progressively increase medium pH, which facilitates the self-assembly of individual  $\text{Fe}_2\text{O}_3$  NPs and forms corresponding SPs (Figures S1 and S2). Figures 1 and 2A are the ultra-large-

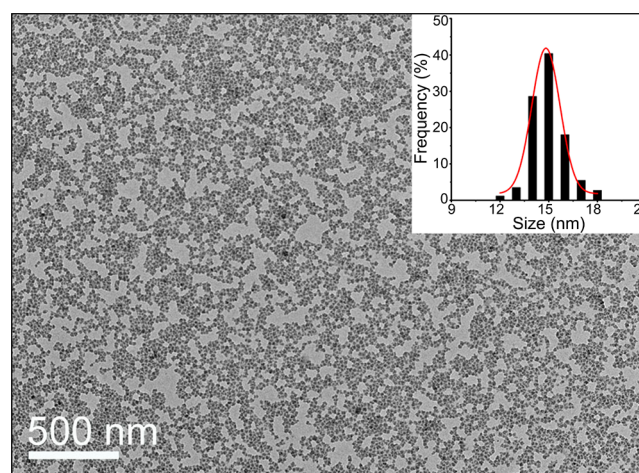


**Figure 1.** Large-scale TEM image of the  $\text{Fe}_2\text{O}_3$  SPs. The inset is the size distribution of the  $\text{Fe}_2\text{O}_3$  SPs, which is based on the statistics of 500 SPs.

and small-scale transmission electron microscopy (TEM) images of the products, respectively. They are 15 nm in diameter, and the size distribution (inset in Figure 1) is as low as 7%. As described by the high-resolution (HR) TEM image (Figure 2B and Figure S5), the products are composed of a few 3–5 nm sized subunits and result in rather rough profiles. Because the present products have a hierarchical structure, they are named as SPs in this contribution. During the self-assembly processes, the NPs' surface energies are easily released and decreased, which is very helpful for enhancing the colloidal stability (see below). Based on the HRTEM result, the as-prepared products do not exhibit distinct lattice fringes (although a few fringes are occasionally observed for parts of the building blocks). Then, the crystallinity of the products was detected by selected area electron diffraction (SAED) and X-ray powder diffraction (XRD) techniques. As shown in Figure 2C, the SAED pattern shows only diffuse rings. Consistently, no obvious diffraction peaks are observed in the XRD pattern (Figure 2D). These results demonstrate that the as-prepared products are predominately amorphous in structure.

Then, the compositions and structures of the products were comprehensively detected. Figure 2E shows the X-ray photoelectron spectroscopy (XPS) measurement for the Fe 2p spectrum. The two peaks at 711.7 and 725.6 eV are attributed to Fe 2p<sub>3/2</sub> and Fe 2p<sub>1/2</sub> of  $\text{Fe}^{3+}$  ions,<sup>19,20</sup> respectively. Furthermore, a satellite at 719.9 eV is rather distinct, which is most pronounced for  $\text{Fe}_2\text{O}_3$ .<sup>21</sup> Based on XPS detection, no information from  $\text{Fe}^{2+}$  has been observed, which would appear at 709.3 eV.<sup>22</sup> X-ray absorption spectroscopy (XAS) is a powerful site-specific local structural probe. Both synchrotron-based X-ray absorption near-edge structure (XANES) and extended X-ray absorption fine structure (EXAFS) in XAS are especially suited for determining local structures of amorphous materials. Figure 2F,G shows the XANES and EXAFS spectra, respectively, and the data for bulk  $\text{Fe}_2\text{O}_3$  and Fe foil are also shown for comparison. It can be seen that the Fe K-edge XANES is very similar to that of  $\text{Fe}_2\text{O}_3$ , indicating that the Fe species have the same valence state as the  $\text{Fe}_2\text{O}_3$  material. Furthermore, more structural information about Fe was obtained by EXAFS. The Fourier transformed (FT)  $k_3$ -weighted EXAFS spectrum (Figure 2G)



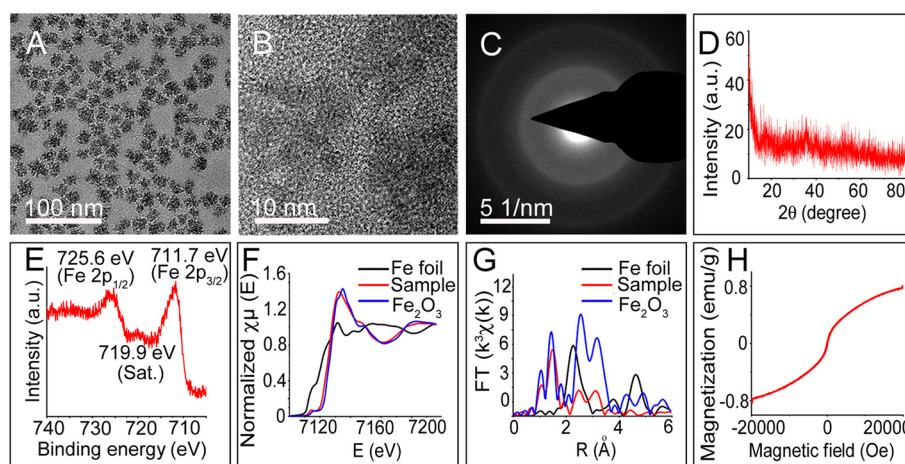


**Figure 2.** Characterizations of the  $\text{Fe}_2\text{O}_3$  SPs. (A) Small-scale TEM image. (B) HRTEM image. (C) SAED and (D) XRD patterns. (E) XPS spectrum of Fe 2p. (F) XANES and (G) EXAFS. (H) Field-dependent magnetization curve.

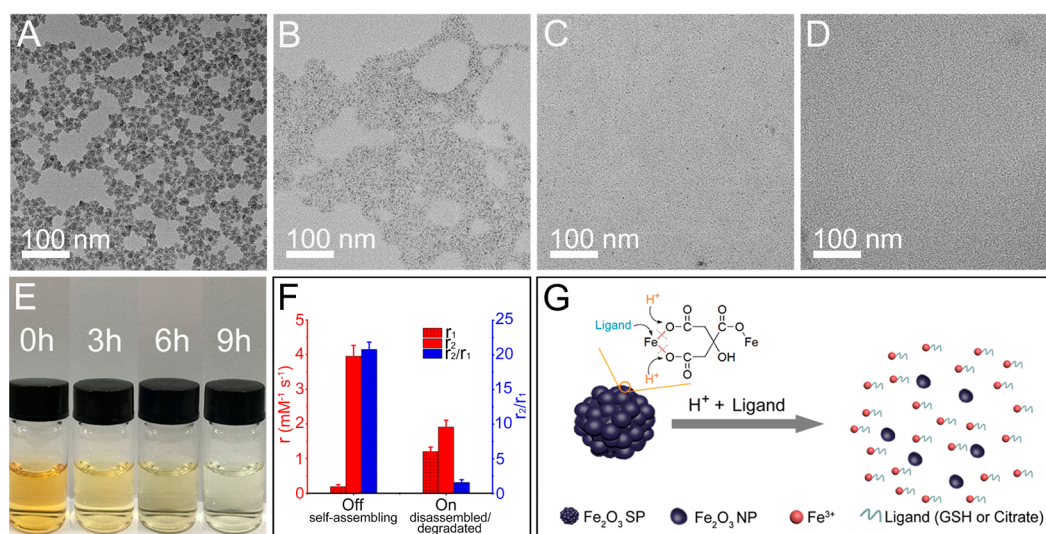


**Figure 3.** *In vitro* disassembly/degradation behaviors and off-on MRI switch. TEM images of the  $\text{Fe}_2\text{O}_3$  SPs in ( $\text{H}^+$  and GSH) system for 0 h (A), 3 h (B), 6 h (C), and 9 h (D). (E) Photo images corresponding to A–D. (F) Relaxivity of the  $\text{Fe}_2\text{O}_3$  SPs in pure water (off) and disassembled/degraded in the ( $\text{H}^+$  + GSH) system for 6 h. (G) Schematic figure for the disassembly/degradation of the  $\text{Fe}_2\text{O}_3$  SPs in the ( $\text{H}^+$  + GSH) system.

of the sample showed three main peaks at 1.5, 2.5, and 3.1 Å,<sup>23,24</sup> corresponding to Fe–O and Fe–Fe<sup>25,26</sup> coordination shells, respectively. Meanwhile, the R spaces of the sample are close to that of  $\text{Fe}_2\text{O}_3$  bulk. Based on that stated above, it can be inferred that the products are  $\text{Fe}_2\text{O}_3$  SPs. It should be noted that the magnetization of the  $\text{Fe}_2\text{O}_3$  SPs is only  $0.78 \text{ emu g}^{-1}$  (Figure 2H), which mainly results from their quasi-amorphous structure.

The *in vitro* relaxivity and its modulation behaviors of the  $\text{Fe}_2\text{O}_3$  SPs were then studied. As shown in Figure 3F, the  $r_1$  and  $r_2$  values of the  $\text{Fe}_2\text{O}_3$  SPs are 0.19 and  $3.95 \text{ mM}^{-1} \text{ s}^{-1}$ , respectively. Herein, because of relatively small surface-to-volume ratio and weak magnetism, the SPs exhibit rather low  $r_1$  relaxivity. As described in Figure 2, the  $\text{Fe}_2\text{O}_3$  SPs possess hierarchical topology and quasi-amorphous structure, which might be disassembled and even degradable at optimal conditions. To address these issues, the  $\text{Fe}_2\text{O}_3$  SPs were dispersed in mediums containing glutathione (GSH, 5 mM),  $\text{H}^+$  ions (citrate buffer solution, 2 mM, pH 5.0), and GSH +  $\text{H}^+$  (GSH, 5 mM; citrate buffer solution, 2 mM, pH 5.0). As

shown in Figure 3E and Figure S10, in all three mediums, the color of the SPs becomes weaker and weaker with the increase of the incubation time. Furthermore, the speeds of the color fading are different in the three systems, namely, ( $\text{GSH} + \text{H}^+$ ) >  $\text{H}^+$  > GSH. These results indicate that the  $\text{Fe}_2\text{O}_3$  SPs are probably disassembled/degradable in these mediums, and ( $\text{GSH} + \text{H}^+$ ) possesses the most prominent effects. Based on TEM detection (Figure 3A–D), the  $\text{Fe}_2\text{O}_3$  SPs are disassembled and even degradable. Herein, the medium of ( $\text{GSH} + \text{H}^+$ ) has the best disassembled/degradable effects, which can be understood as follows: The as-prepared  $\text{Fe}_2\text{O}_3$  SPs are self-assembled by 3–5 nm sized  $\text{Fe}_2\text{O}_3$  NPs, and the cross-linking effects of carboxyl groups within citrate molecules among the nanocrystals probably play an important role in the self-assembly.<sup>27</sup> The added  $\text{H}^+$  ions and ligands (citrate and GSH molecules) can “attack” carboxyl groups and  $\text{Fe}^{3+}$  ions (Figure S9), respectively, which causes the disassembly/degradation of the  $\text{Fe}_2\text{O}_3$  SPs (Figure 3G). Due to enhanced “attack” effects, ( $\text{H}^+$  + GSH) medium possesses the best performances for the disassembly/degradation. Accompanied



by the disassembly/degradation behaviors, the  $r_1$  value increases from 0.19 to 1.20  $\text{mM}^{-1} \text{S}^{-1}$ , and the  $r_2/r_1$  value decreases from 20.79 to 1.59 (Figure 3F). Then, the effects of a few experimental parameters, such as reaction time and pH values, on the disassembly/degradation of the  $\text{Fe}_2\text{O}_3$  SPs were further investigated. As shown in Figure S11, even only at 30 min reaction, an apparent size decrease of the  $\text{Fe}_2\text{O}_3$  SPs is observed; at the same time, the  $r_1$  value increases more than 3 times (from 0.19 to 0.61  $\text{mM}^{-1} \text{S}^{-1}$ ), whereas the  $r_2/r_1$  ratio decreases from 20.79 to 5.23. Furthermore, such disassembly/degradation processes can smoothly proceed in pH 6.2 medium, and only the reaction speed exhibits some decrease (Figure S12).

It should be noted that such stimulation-induced disassembled/degradable behaviors have three advantages for MRI imaging *in vivo*, although *in vivo* situations are very different from those *in vitro*. First, due to the substantial increase of the surface-to-volume ratio, the disassembly/degradation of the  $\text{Fe}_2\text{O}_3$  SPs causes a more than 6 times enhancement of  $r_1$  relaxivity. In fact, in addition to the disassembly/degradation effects, a lower pH value is also helpful for enhancing the relaxivity, as shown in Figure S13. The possible reason is that lower pH values facilitate the coordination interactions of water molecules and particle surface, and then higher  $r_1$  values are obtained.<sup>28</sup> Second, the best disassembled/degradable condition, namely, (GSH +  $\text{H}^+$ ) medium, is just the microenvironment for most tumors. So, the present  $\text{Fe}_2\text{O}_3$  SPs, due to their distinctly active  $r_1$  relaxivity toward the tumor microenvironment, are promising for enhancing the signal-to-noise ratio for the corresponding MRI imaging. Third, the  $\text{H}^+$ /ligand-induced disassembly/degradation can also be conducted in lysosome (Figure S14), which is essential for their clearance/excretion from living bodies in time (see below).

In the following, the *in vivo* MRI performances of the  $\text{Fe}_2\text{O}_3$  SPs were studied. To avoid their potential aggregation in biological systems, the SPs were then modified with bovine serum albumin (BSA) molecules for various biologically related experiments. After BSA modification, the dynamic light scattering (DLS) size of the  $\text{Fe}_2\text{O}_3$  SPs exhibits some increase (from 15.69 to 21.04 nm, Figure S15). To estimate their biological applications, the cell uptake and cell cytotoxicity tests were first conducted. Based on inductively coupled plasma mass spectrometry (ICP-MS) detection, the cellular uptake gradually increased with the enhancement of incubation time. At 24 h incubation, the uptake value is 70 pg of iron for per cell (Figure S17), which is slightly higher than that of the 6 nm sized poly(L-lysine)-modified  $\text{Fe}_2\text{O}_3$  (41 pg/cell).<sup>29–31</sup> Based on CCK-8 assay (Figure S18), the cell viability can exceed 94% even if the concentration of the incubated  $\text{Fe}_2\text{O}_3$  SPs is as high as 600  $\mu\text{g mL}^{-1}$  (in the present contribution, all concentrations of the  $\text{Fe}_2\text{O}_3$  SPs were estimated by  $\text{Fe}^{3+}$  ions). These results indicate that the  $\text{Fe}_2\text{O}_3$  SPs have low toxicity and are highly biocompatible.

The MRI performances of the  $\text{Fe}_2\text{O}_3$  SPs *in vivo* were evaluated in a subcutaneous 4T1 breast tumor model using a BioSpec70/20USR 7 T MRI scanner. Whole-body MR images were obtained 10 min, 30 min, 1 h, 1.5 h, 2 h, 4 h, and 24 h after the intravenous injection of the  $\text{Fe}_2\text{O}_3$  SPs (100  $\mu\text{L}$ , 3.75  $\text{mg mL}^{-1}$ ). As shown in Figure 4A, a distinct  $T_1$ -weighted signal is observed within the tumor area 10 min after intravenous injection of the  $\text{Fe}_2\text{O}_3$  SPs. This intense signal is then gradually decreased and nearly disappears in the following

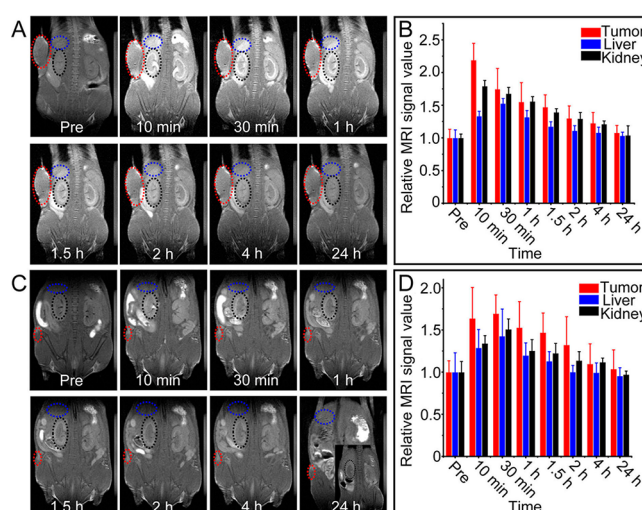


**Figure 4.** Time-dependent *in vivo* MRI images of 4T1-tumor-bearing nude mice after intravenous injection of the  $\text{Fe}_2\text{O}_3$  SPs at different time intervals. For A, B and C, D, the tumor sizes are about 300 and 5  $\text{mm}^3$ , respectively. In A and C, the tumor, liver, and kidney are circled by red, blue, and black ellipses, respectively. The corresponding MRI intensities of A (B) and C (D) at the tumor, liver, and kidney. The dose of the injected  $\text{Fe}_2\text{O}_3$  SPs is 0.375 mg (100  $\mu\text{L}$ , 3.75  $\text{mg mL}^{-1}$ ).

24 h (Figure 4A,B). Meanwhile, the MRI signals of liver and kidney organs are monitored. The signal from the kidney is somewhat higher than that of the liver, indicating that renal clearance probably plays an important role in the SPs' elimination. Similar with the tumor site, the signals at the two organs reach the maximum within 10 min, which then gradually decreases and almost completely recovers at 24 h. To further evaluate their tumor-targeting ability, the  $\text{Fe}_2\text{O}_3$  SPs were injected into the tail vein of nude mice bearing a small sized tumor ( $\sim 5 \text{ mm}^3$  in volume). The clear MRI signal can be observed at the tumor site (Figure 4C), indicating the potential applications of the  $\text{Fe}_2\text{O}_3$  SPs for early tumor diagnosis. Obviously, the off-on switchable MRI properties, especially in the tumor microenvironment that induced an active  $T_1$ -weighted signal, are pivotal for high-performance imaging.

To better understand the clearance behaviors of the as-prepared  $\text{Fe}_2\text{O}_3$  SPs, healthy mice were then adopted for the relevant experiments. After intravenous tail injection (100  $\mu\text{L}$ , 3.75  $\text{mg mL}^{-1}$ ), the MRI signals of the liver, kidney, as well as bladder were continuously monitored. As shown in Figure 5A, the intensity of MRI signals at the kidneys and liver is distinctly enhanced after 10 min injection, and the signal intensity at the kidneys is about 20% higher than that at the liver. Furthermore, the signal intensities in both organs can be maintained for several subsequent hours despite some gradual decrease. Twelve hours after injection, their MRI signals almost completely recover to that of their predose. Overall, the MRI evolution is similar to that of the tumor-bearing mice. Then, the MRI signals at the bladder were continuously detected. As shown in Figure 5C, the evolution of MRI signals at the bladder is rather coincident with that at the liver and kidneys, and only the intensities are much higher than that of the two organs. On this basis, it is clear that the as-proposed  $\text{Fe}_2\text{O}_3$  SPs are mainly excreted by renal clearance.

At present, it is widely believed that the injected NPs are excreted by renal clearance as their hydrodynamic diameter is



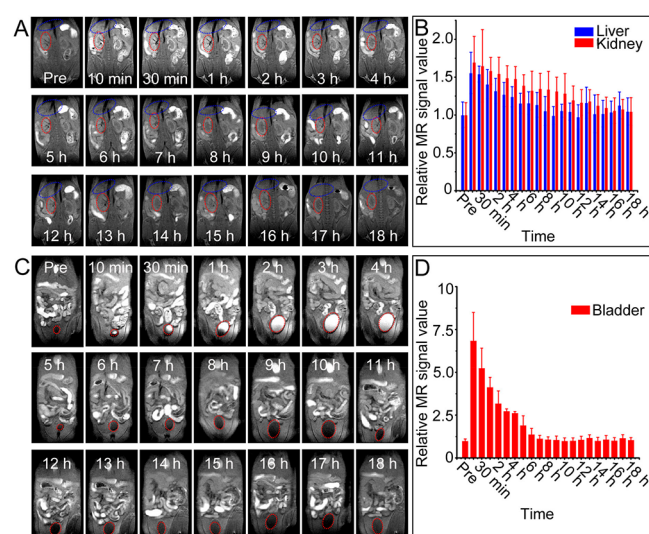


**Figure 5.** Time-dependent *in vivo* MRI of liver, kidneys, and bladder of healthy nude mice after the injection of the  $\text{Fe}_2\text{O}_3$  SPs ( $100\ \mu\text{L}$ ,  $3.75\ \text{mg mL}^{-1}$ ). (A) *In vivo* MRI images of a healthy nude mouse after intravenous injection (liver, blue ellipses; kidney, red ellipses) of the 15 nm sized BSA-modified  $\text{Fe}_2\text{O}_3$  SPs at different time intervals. (B) Corresponding data at the liver and kidneys. (C) *In vivo* MRI images of a healthy nude mouse after intravenous injection (bladder, red ellipses) of the 15 nm sized BSA-modified  $\text{Fe}_2\text{O}_3$  SPs at different time intervals. (D) Corresponding data at the bladder.

less than  $\sim 6\text{--}8\ \text{nm}$ .<sup>32–34</sup> Herein, the DLS size of the BSA-modified  $\text{Fe}_2\text{O}_3$  SPs are greater than 20 nm, which is obviously larger than that of glomerular filtration membranes. So, the following questions are whether the  $\text{Fe}_2\text{O}_3$  SPs can adequately disassemble and degrade in time for the renal clearance and whether the clearance causes kidney damage. To unravel these issues, we investigated kidney function and kidney structures of the mice after being exposed to the  $\text{Fe}_2\text{O}_3$  SPs. Two renal function markers, namely, blood urea nitrogen and serum creatinine,<sup>35</sup> were monitored 14 days after intravenous injection of the  $\text{Fe}_2\text{O}_3$  SPs into the mice ( $100\ \mu\text{L}$ ,  $3.75\ \text{mg mL}^{-1}$ ). As shown in Figure 6C,D, no distinct changes in both blood urea nitrogen and serum creatinine levels are observed from 1 to 14 days, compared with that of noninjected mice. For better assessment, renal histopathology studies were then conducted. As shown in Figure 6E–H, the section of the kidney, with both  $\text{Fe}_2\text{O}_3$  SPs injected mice and the control one, shows the presence of a renal corpuscle surrounded by Bowman's capsule; then, kidney tubules are lined with simple cuboidal epithelium. Furthermore, the glomerulus, a tuft of capillaries, also appears as a large cellular mass.<sup>36</sup> In addition, to further study the glomerular status, the ultrastructural examination for glomerular endothelium and podocyte foot processes was detected by TEM. As shown in Figure 6I–P, podocyte morphology exhibits no changes after the injection of the  $\text{Fe}_2\text{O}_3$  SPs from 1 to 14 days, indicating that the  $\text{Fe}_2\text{O}_3$  SPs do not cause damage to the endothelium and normal podocyte foot processes. Also, both the glomeruli and glomerular filtration membranes remain rather normal.<sup>35,37,38</sup> By combination of the above data, it is clear that the renal clearance processes of the  $\text{Fe}_2\text{O}_3$  SPs do not cause kidney damage. In addition to *in vitro* experiments (Figure 3 and Figure S14), the urine from an injected mouse was collected, treated, and detected by TEM. As shown in Figure 6A,B, well-defined 2–5

nm NPs are observed in the urea samples. These data, from both *in vitro* and *in vivo*, demonstrate that the proposed  $\text{Fe}_2\text{O}_3$  SPs can disassemble/decompose into 3–5 nm sized individual NPs and even small molecule complexes, which are small enough for glomerular filtration barriers and excretion by renal clearance. As shown in Figure S19, as the dose of the injected  $\text{Fe}_2\text{O}_3$  SPs is increased to  $1.0\ \text{mg}$  ( $100\ \mu\text{L}$ ,  $10\ \text{mg mL}^{-1}$ ), slight kidney damage is observed by H&E-stained images, although the levels of blood urea nitrogen and serum creatinine are normal. Obviously, the injected dosage is one of critical parameters for the corresponding applications.

In the following, as a comparison, the MRI performances and elimination behaviors of the 4 nm sized  $\text{Fe}_2\text{O}_3$  NPs (unassembled products) were then studied. As shown in Figure S20, the slightly large tumor ( $20\ \text{mm}^3$ ) was imaged by  $T_1$ -weighted signals using the unassembled  $\text{Fe}_2\text{O}_3$  NPs as contrast agents. However, the NPs tend to accumulate at the liver, as described by distinctly black  $T_2$ -weighted signals, even after 48 h injection (blue circles in Figure S20A). In contrast, the  $T_1$ -weighted signals at the bladder only exhibit a small enhancement throughout (red circles in Figure S21). These preliminary results indicate that the unassembled  $\text{Fe}_2\text{O}_3$  NPs are probably cleared by the liver. The possible reason is that the  $\text{Fe}_2\text{O}_3$  NPs heavily aggregate during blood circulation, which then are captured by macrophagocytes of the liver. Because the interaction of injected nanomaterials and living bodies is extremely complex, the exact processes need further research.

To further understand the pharmacokinetic behaviors of the  $\text{Fe}_2\text{O}_3$  SPs, the urine and feces of the injected mice were collected and measured by ICP. As shown in Figure S22, high levels of Fe were detected in the urine, particularly in the first 4 h; soon afterward, Fe levels in urine drastically decreased. For the feces samples, despite the decreasing speed being obviously lower than that in urine, Fe levels also reach a rather low value after 3 days. These results indicate that Fe can be quickly excreted from the body. It should be noted that the Fe contents in urine are higher than that in feces at 1 day. In this regard, renal clearance plays a major role in the excretion of  $\text{Fe}_2\text{O}_3$  SPs, which is in good agreement with the results of MRI detection (Figure 5). Next, the clearance of the  $\text{Fe}_2\text{O}_3$  SPs is investigated by measuring the Fe contents in major organs, namely, heart, liver, spleen, lungs, and kidneys, of mice at different time points post i.v. injection of the SPs ( $100\ \mu\text{L}$ ,  $10\ \text{mg mL}^{-1}$ ). As shown in Figure S23, Fe levels in all measured organs rapidly decreased after only 1.5 h to 1 day injection. Importantly, after 3–7 days, Fe levels in these organs became very low, demonstrating that the as-prepared  $\text{Fe}_2\text{O}_3$  SPs can be excreted from living bodies in a short time. So, the present  $\text{Fe}_2\text{O}_3$  SPs can probably avoid long-term retention/toxicity, which is one of the biggest concerns for various nano-medicines.

Finally, in order to evaluate whether the  $\text{Fe}_2\text{O}_3$  SPs are potentially toxic, complete necropsies and hematology are conducted based on humanely euthanized control and treated mice. The major organs including heart, liver, spleen, lungs, and kidneys were examined at 20 min, 1.5 h, 1 day, 7 days, and 30 days postinjection of the  $\text{Fe}_2\text{O}_3$  SPs ( $100\ \mu\text{L}$ ,  $10\ \text{mg mL}^{-1}$ ). The histopathology shown in Figure S25 reveals no obvious organ abnormalities and/or lesions for the mice treated with  $\text{Fe}_2\text{O}_3$  SPs, as compared with the control group. Furthermore, abnormalities of red/white blood cells or serum chemistry are also not detected (Figure S26), which is often relevant with



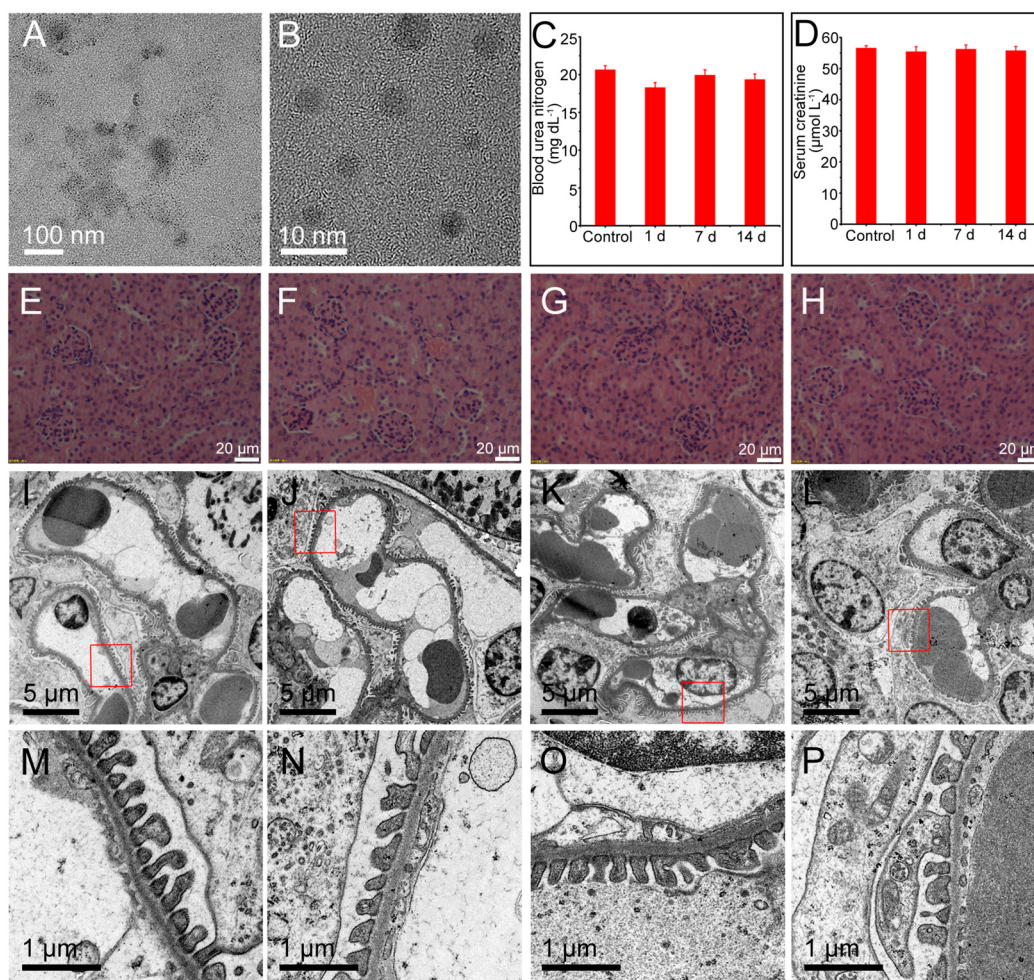


**Figure 6.** Evaluating renal function and tissue structures of kidneys for mice injected with Fe<sub>2</sub>O<sub>3</sub> SPs. (A) TEM and (B) HRTEM images of a mouse's urine after injection with the Fe<sub>2</sub>O<sub>3</sub> SPs. Levels of urea (C) and creatinine (D) in plasma of the mice after injection with the Fe<sub>2</sub>O<sub>3</sub> SPs for various times. H&E-stained images of the kidney collected from the mice of the control one (E) and after injection with the Fe<sub>2</sub>O<sub>3</sub> SPs for 1 day (F), 7 days (G), and 14 days (H). TEM images of glomeruli collected from the mice of control one (I,M) and after injection with the Fe<sub>2</sub>O<sub>3</sub> SPs for 1 day (J,N), 7 days (K,O), and 14 days (L,P). Panels M, N, O, and P are the amplification of the areas highlighted by the red squares in I, J, K, and L, respectively. The dose of the injected Fe<sub>2</sub>O<sub>3</sub> SPs is 0.375 mg (100 μL, 3.75 mg mL<sup>-1</sup>).

organ damage and/or inflammation. In addition, for the hematology assessment, other markers such as platelet count and hematocrit did not show differences, all within normal range. Liver function markers including alanine aminotransferase, aspartate aminotransferase, and total protein of mice after Fe<sub>2</sub>O<sub>3</sub> SP treatment showed a slight variation compared with those of the control group but were kept within the normal range. So, there was no obvious hepatic toxicity. According to the above systematic animal toxicity evaluation, the Fe<sub>2</sub>O<sub>3</sub> SPs are highly biocompatible even at the *in vivo* level, which is probably competent as one of the MRI agents possessing clinical application potentials.

## CONCLUSIONS

In summary, we fabricate monodisperse Fe<sub>2</sub>O<sub>3</sub> SPs in aqueous medium and systematically study their *in vivo* T<sub>1</sub>-weighted MRI performances, biodistribution, as well as metabolic behaviors. By virtue of their quasi-amorphous and hierarchical structures, the proposed Fe<sub>2</sub>O<sub>3</sub> SPs not only possess high signal-to-noise ratio but also exhibit a few favorable properties (biocompatibility, biodegradability, easy clearance) in biological applications. This contribution, on the one hand,

provides a very promising contrast agent for MRI applications; on the other hand, it demonstrates that the crystallinity and topological design have profound effects on the biological effects/performances of nanomedicines.

## METHODS

**Materials.** FeCl<sub>3</sub>·6H<sub>2</sub>O and NaOH were purchased from Sinopharm Chemical Reagent Co., Ltd. (Shanghai, China). Sodium citrate dihydrate and citric acid were obtained from Alfa Aesar (Tianjin, China). Urea was bought from Sigma-Adrich Co., Ltd. (Shanghai, China). Roswell Park Memorial Institute (RPMI-1640), fetal bovine serum, penicillin, and streptomycin were obtained from Gibco Invitrogen Co., Ltd. (New York, USA). BSA and GSH were acquired from BBI Life Sciences Co., Ltd. (Shanghai, China). All chemicals were used without purification.

**Instruments.** The morphology of Fe<sub>2</sub>O<sub>3</sub> SPs was detected by transmission electron microscopy on a Tecnai G2 20 ST (FEI, USA) under an accelerating voltage of 200 kV. High-resolution TEM was performed using a G2 F20 U-TWIN (FEI, USA) TEM operating at 200 kV. The hydrodynamic particle size and ζ-potential values were examined on a Zetasizer Nano ZS series instrument (Malvern Instruments Co., Ltd., UK) with 633 nm laser wavelength and a measurement angle of 173° (backscatter detection) at 25 °C. Fourier transform infrared spectra (4000–400 cm<sup>-1</sup>) were recorded by a



Magna-560 spectrometer (Nicolet, Madison, WI, USA). X-ray diffraction measurements were performed on a D8 Focus XRD system (Bruker, Germany). X-ray photoelectron spectroscopy was obtained on an ESCALAB 250Xi photoelectron spectrometer (Thermo Fisher Scientific, USA). X-ray absorption fine structure and extended XAFS spectra were obtained at the 1W1B station in BSRF (Beijing Synchrotron Radiation Facility, China) operated with the U-SPECT+/CT imaging system (MILABS, The Netherlands). Magnetic measurements were performed with a PPMS-9 superconducting quantum interference device (SQUID) magnetometer (Quantum Design, USA). The measurements were recorded between  $-20000$  and  $20000$  Oe at  $300$  K. Magnetic resonance imaging (MRI,  $7$  T) was performed with a BioSpec70/20USR spectrometer (Bruker, Germany). Blood biochemistry analysis was obtained on a Chemray 240 hematology analyzer (Rayto, China). Cell viability was determined by a Varioskan Flash microplate reader (Thermo Fisher Scientific, USA). Fe contents in all samples were determined by inductively coupled plasma mass spectrometry on a NexION 300X instrument (PerkinElmer, USA). Kidney ultrastructural detection was conducted by TEM on HT7700 (Hitachi, Japan) at  $80$  kV accelerating voltage. H&E staining was done using a EVOS XL core digital microscope (Life Technologies, USA).

**Fabrication and Purification of the  $\text{Fe}_2\text{O}_3$  SPs.** Sodium citrate dihydrate ( $0.1$  g) and  $\text{FeCl}_3 \cdot 6\text{H}_2\text{O}$  ( $0.045$  g) were dissolved in  $100$  mL of deionized water in a  $250$  mL three-necked flask under vigorous stirring, followed by adjustment of the pH to  $5.8$  with NaOH solution ( $0.1$  mol  $\text{L}^{-1}$ ). Then,  $0.024$  g of urea was added to the above solution, which was heated to  $100$  °C and refluxed for  $24$  h. When the reaction was finished, the solution of  $\text{Fe}_2\text{O}_3$  SPs was cooled naturally to room temperature. To purify the  $\text{Fe}_2\text{O}_3$  SPs, for  $2$  mL of the crude solution containing the SPs,  $6$  mL of isopropyl alcohol was added and mixed adequately, which was then centrifuged at  $10000$  rpm for  $10$  min. The obtained precipitates were redispersed into water solution and/or freeze-dried for various characterizations and/or biological applications.

**In Vitro Disassembly/Degradation Experiments.** In order to explore the experimental factors on the disassembly/degradation behaviors of the  $\text{Fe}_2\text{O}_3$  SPs. Two milliliters of the solutions containing crude  $\text{Fe}_2\text{O}_3$  SPs (four copies) was centrifuged at  $10000$  rpm for  $10$  min to purify the SPs. The obtaining precipitates were dispersed into pure  $\text{H}_2\text{O}$  solution ( $4$  mL, pH  $7.0$ ), GSH solution ( $4$  mL,  $5$  mM, pH  $7.0$ ),  $\text{H}^+$  solution ( $4$  mL, sodium citrate buffer solution,  $2$  mM, pH  $5.0$ ), (GSH +  $\text{H}^+$ ) solution ( $4$  mL, GSH:  $5$  mM; sodium citrate buffer solution,  $2$  mM, pH  $5.0$ ), (GSH +  $\text{H}^+$ ) solution ( $4$  mL, GSH:  $5$  mM; sodium citrate buffer solution,  $2$  mM, pH  $6.2$ ), and phosphate-buffered saline solution (pH  $7.4$ ). Then all the mixed solutions were shaken at  $37$  °C at  $100$  rpm in a shaker, which were detected by TEM and/or taking photos at different time intervals for monitoring their reactions.

To better understand the disassembly/degradation of the  $\text{Fe}_2\text{O}_3$  SPs, the purified  $\text{Fe}_2\text{O}_3$  SPs were further dispersed into artificial lysosomal liquid, and the final concentration of the  $\text{Fe}_2\text{O}_3$  SPs was  $2$  mM. Then, the mixture was kept at  $37$  °C. Samples were taken at intervals of  $24$  h for TEM characterizations. Preparation of artificial lysosomal liquid solution:  $3.210$  g of NaCl,  $6.000$  g of NaOH,  $20.800$  g of citric acid,  $0.097$  g of  $\text{CaCl}_2$ ,  $0.197$  g of  $\text{Na}_2\text{H}_2\text{PO}_4 \cdot 7\text{H}_2\text{O}$ ,  $0.039$  g of  $\text{Na}_2\text{SO}_4$ ,  $0.106$  g of  $\text{MgCl}_2 \cdot 6\text{H}_2\text{O}$ ,  $0.059$  g of glycerol,  $0.077$  g of sodium citrate dehydrated,  $0.090$  g of sodium tartrate dehydrated,  $0.085$  g sodium lactate,  $0.086$  g of sodium pyruvate,  $1.000$  mL of formaldehyde, plus deionized water to  $1$  L.

**Animal Model.** Female BALB/c nude mice and female BALB/c mice ( $5$  weeks old) were purchased from Beijing Weitong Lihua Co., Ltd. Animal experiments were reviewed by the National Nanoscience Center Animal Ethics Committee. The  $4\text{T}1$  tumor model was constructed by subcutaneously injecting the  $4\text{T}1$  cell suspension ( $100$   $\mu\text{L}$ , about  $2 \times 10^5$  cells) into nude mice. Mouse MRI was performed when the tumor volumes reached  $300$ ,  $5$ , and  $20$   $\text{mm}^3$ .

**In Vivo MRI.**  $4\text{T}1$ -tumor-bearing mice were anesthetized by being intraperitoneally injected with  $1\%$  sodium pentobarbital. Subsequently, isoflurane was maintained at  $1.5\%$  for the mice. BSA-

modified  $\text{Fe}_2\text{O}_3$  SPs ( $15$  nm in diameter,  $100$   $\mu\text{L}$ ,  $3.75$  mg  $\text{mL}^{-1}$ ) or BSA-modified  $\text{Fe}_2\text{O}_3$  NPs ( $4$  nm in diameter,  $100$   $\mu\text{L}$ ,  $3.75$  mg  $\text{mL}^{-1}$ ) were intravenously injected into the  $4\text{T}1$ -tumor-bearing mice. Then,  $T_1$ -weighted MRI of the injected mice at different time periods was tested using Bruker's small animal nuclear magnetic resonance spectroscopy ( $7.0$  T,  $\text{TE} = 5.2$  ms,  $\text{TR} = 300$  ms).

**Kidney Ultrastructural Examination.** Two mice in each group were used for the TEM study on glomerular ultrastructure. One group was injected with PBS ( $100$   $\mu\text{L}$ ) via the tail vein. The other three groups of mice (named as  $1$ ,  $7$ , and  $14$  day groups) were intravenously injected with the BSA-modified  $\text{Fe}_2\text{O}_3$  SPs ( $15$  nm in diameter,  $100$   $\mu\text{L}$ ,  $3.75$  mg  $\text{mL}^{-1}$ ). The mice of both groups were euthanized at corresponding time points for short-term and long-term kidney injury examination. Kidney tissue samples were fixed for  $2$  h in a mixture of  $2.5\%$  glutaraldehyde in PBS ( $0.1$  M, pH  $7.2$ ). The samples were postfixed, embedded, and dyed. Then the grids were observed in a HT7700 TEM at  $80$  kV accelerating voltage.

**In Vivo Biodistribution, Toxicity, and Metabolism Test.** Healthy female BALB/c mice were divided into six groups (five mice in each group). One group was injected with PBS ( $100$   $\mu\text{L}$ ) via the tail vein. The other five groups of mice (named as  $20$  min group,  $1.5$  h group,  $1$  day group,  $7$  days group, and  $30$  days group) were intravenously injected with the BSA-modified  $\text{Fe}_2\text{O}_3$  SPs ( $15$  nm in diameter,  $100$   $\mu\text{L}$ ,  $10$  mg  $\text{mL}^{-1}$ ). Body weight changes of the control group and the  $30$  day group were recorded every day. Blood was collected from the mice, then whole blood ( $60$   $\mu\text{L}$ ) underwent hematological analysis. In addition, the rest of the blood sample was kept at  $37$  °C for  $2$  h and then centrifuged at  $3000$  rpm for  $15$  min. The supernatant serum was stored at  $-80$  °C for biochemistry analysis using a hematology analyzer (Chemray 240). To study histopathology, the mice were sacrificed and the heart, liver, spleen, lungs, and kidneys were fixed with  $4\%$  paraformaldehyde tissue fixative, embedded in paraffin, and sectioned into slices. Then, H&E staining for pathological analysis was conducted. To investigate the biodistribution of Fe, the major organs including heart, liver, spleen, lungs, and kidneys were weighed and digested with concentrated nitric acid, and Fe contents were measured by ICP-MS.

To study the *in vivo* excretion pathway, five healthy BALB/c mice were placed in the metabolism cages and injected with the BSA-modified  $\text{Fe}_2\text{O}_3$  SPs ( $15$  nm in diameter,  $100$   $\mu\text{L}$ ,  $10$  mg  $\text{mL}^{-1}$ ). Urine and feces were collected at various time periods, which were digested with concentrated nitric acid. After digestion, the contents of Fe in each sample were tested by ICP-MS. In addition, the urine was dialyzed for  $48$  h for TEM characterization.

## ASSOCIATED CONTENT

### Supporting Information

The Supporting Information is available free of charge at <https://pubs.acs.org/doi/10.1021/acsnano.9b08570>.

Fabrication of the  $4$  nm sized  $\text{Fe}_2\text{O}_3$  NPs,  $\text{Fe}_2\text{O}_3$  NPs using NaOH for pH modulation, and the BSA-modified  $\text{Fe}_2\text{O}_3$  SPs; the  $\zeta$ -potential values and TEM images of the  $\text{Fe}_2\text{O}_3$  SPs fabricated by a citrate-urea system and a citrate-NaOH system; HRTEM image of the  $\text{Fe}_2\text{O}_3$  SPs; XPS spectrum of O  $1s$ ; stability of the  $\text{Fe}_2\text{O}_3$  SPs; Fourier transform infrared spectra of GSH, the  $\text{Fe}_2\text{O}_3$  SPs, and GSH-induced disassembled SPs; TEM images and the relaxivity of the  $\text{Fe}_2\text{O}_3$  SPs in the medium of ( $\text{H}^+$  + GSH) solution; cell uptake and cell viability; H&E-stained images of kidney; *in vivo* time-dependent MRI of tumor, liver, kidney, and bladder ( $4$  nm sized BSA modified  $\text{Fe}_2\text{O}_3$  NPs); *in vivo* biodistribution of the BSA-modified  $\text{Fe}_2\text{O}_3$  SPs; H&E-stained images of major organs; blood analysis of the  $\text{Fe}_2\text{O}_3$  SPs (PDF)



## AUTHOR INFORMATION

## Corresponding Author

Yunsheng Xia – Key Laboratory of Functional Molecular Solids, Ministry of Education, College of Chemistry and Materials Science, Anhui Normal University, Wuhu 241000, China; [orcid.org/0000-0002-7877-9718](https://orcid.org/0000-0002-7877-9718); Phone: +86-553-3869303; Email: [xiayuns@mail.ahnu.edu.cn](mailto:xiayuns@mail.ahnu.edu.cn); Fax: +86-553-3869303

## Authors

Mingrou Ma – Key Laboratory of Functional Molecular Solids, Ministry of Education, College of Chemistry and Materials Science, Anhui Normal University, Wuhu 241000, China

Hui Zhu – Key Laboratory of Functional Molecular Solids, Ministry of Education, College of Chemistry and Materials Science, Anhui Normal University, Wuhu 241000, China

Jing Ling – Key Laboratory of Functional Molecular Solids, Ministry of Education, College of Chemistry and Materials Science, Anhui Normal University, Wuhu 241000, China

Suqin Gong – Key Laboratory of Functional Molecular Solids, Ministry of Education, College of Chemistry and Materials Science, Anhui Normal University, Wuhu 241000, China

Yin Zhang – CAS Key Laboratory of Nanosystem and Hierarchical Fabrication, CAS Center for Excellence in Nanoscience, National Center for Nanoscience and Technology, Beijing 100190, China

Zhiyong Tang – CAS Key Laboratory of Nanosystem and Hierarchical Fabrication, CAS Center for Excellence in Nanoscience, National Center for Nanoscience and Technology, Beijing 100190, China; [orcid.org/0000-0003-0610-0064](https://orcid.org/0000-0003-0610-0064)

Complete contact information is available at: <https://pubs.acs.org/10.1021/acsnano.9b08570>

## Notes

The authors declare no competing financial interest.

## ACKNOWLEDGMENTS

This work is financially supported by the National Natural Science Foundation of China (Nos. 21775004 and 21422501) and Wanjiaang Scholar program.

## REFERENCES

- (1) Qiao, R.; Yang, C.; Gao, M. Superparamagnetic Iron Oxide Nanoparticles: From Preparations to *In Vivo* MRI Applications. *J. Mater. Chem.* **2009**, *19*, 6274–6293.
- (2) El-Boubbou, K. Magnetic Iron Oxide Nanoparticles as Drug Carriers: Clinical Relevance. *Nanomedicine* **2018**, *13*, 953–971.
- (3) Bulte, J. W. M.; Kraitchman, D. L. Iron Oxide MR Contrast Agents for Molecular and Cellular Imaging. *NMR Biomed.* **2004**, *17*, 484–499.
- (4) Li, Z.; Yi, P. W.; Sun, Q.; Lei, H.; Li Zhao, H.; Zhu, Z. H.; Smith, S. C.; Lan, M. B.; Lu, G. Q. M. Ultrasmall Water-Soluble and Biocompatible Magnetic Iron Oxide Nanoparticles as Positive and Negative Dual Contrast Agents. *Adv. Funct. Mater.* **2012**, *22*, 2387–2393.
- (5) Bobo, D.; Robinson, K. J.; Islam, J.; Thurecht, K. J.; Corrie, S. R. Nanoparticle-Based Medicines: A Review of FDA-Approved Materials and Clinical Trials to Date. *Pharm. Res.* **2016**, *33*, 2373–2387.
- (6) Penfield, J. G.; Reilly, R. F. What Nephrologists Need to Know about Gadolinium. *Nat. Clin. Pract. Nephrol.* **2007**, *3*, 654–668.
- (7) Henderson, L.; Neumann, O.; Kaffes, C.; Zhang, R.; Marangoni, V.; Ravoori, M. K.; Kundra, V.; Bankson, J.; Nordlander, P.; Halas, N. J. Routes to Potentially Safer T<sub>1</sub> Magnetic Resonance Imaging Contrast in a Compact Plasmonic Nanoparticle with Enhanced Fluorescence. *ACS Nano* **2018**, *12*, 8214–8223.
- (8) Silva, A. C.; Lee, J. H.; Aoki, I.; Koretsky, A. P. Manganese-Enhanced Magnetic Resonance Imaging (MEMRI): Methodological and Practical Considerations. *NMR Biomed.* **2004**, *17*, 532–543.
- (9) Lee, J. H.; Silva, A. C.; Merkle, H.; Koretsky, A. P. Manganese-Enhanced Magnetic Resonance Imaging of Mouse Brain after Systemic Administration of MnCl<sub>2</sub>: Dose-Dependent and Temporal Evolution of T<sub>1</sub> Contrast. *Magn. Reson. Med.* **2005**, *53*, 640–648.
- (10) Kim, T.; Momin, E.; Choi, J.; Yuan, K.; Zaidi, H.; Kim, J.; Park, M.; Lee, N.; McMahon, M. T.; Quinones-Hinojosa, A.; Bulte, J. W. M.; Hyeon, T.; Gilad, A. A. Mesoporous Silica-Coated Hollow Manganese Oxide Nanoparticles as Positive T<sub>1</sub> Contrast Agents for Labeling and MRI Tracking of Adipose-Derived Mesenchymal Stem Cells. *J. Am. Chem. Soc.* **2011**, *133*, 2955–2961.
- (11) Peng, Y. K.; Tseng, Y. J.; Liu, C. L.; Chou, S. W.; Chen, Y. W.; Tsang, S. C. E.; Chou, P. T. One-Step Synthesis of Degradable T<sub>1</sub>-FeOOH Functionalized Hollow Mesoporous Silica Nanocomposites from Mesoporous Silica Spheres. *Nanoscale* **2015**, *7*, 2676–2687.
- (12) Bourquin, J.; Milosevic, A.; Hauser, D.; Lehner, R.; Blank, F.; Petri-Fink, A.; Rothen-Rutishauser, B. Biodistribution, Clearance, and Long-Term Fate of Clinically Relevant Nanomaterials. *Adv. Mater.* **2018**, *30*, 1704307.
- (13) Yang, G.; Phua, S. Z. F.; Bindra, A. K.; Zhao, Y. Degradability and Clearance of Inorganic Nanoparticles for Biomedical Applications. *Adv. Mater.* **2019**, *31*, 1805730.
- (14) Viger, M. L.; Sankaranarayanan, J.; de Gracia Lux, C.; Chan, M.; Almutairi, A. Collective Activation of MRI Agents via Encapsulation and Disease-Triggered Release. *J. Am. Chem. Soc.* **2013**, *135*, 7847–7850.
- (15) Yi, Z.; Luo, Z.; Barth, N. D.; Meng, X.; Liu, H.; Bu, W. B.; All, A.; Vendrell, M.; Liu, X. *In Vivo* Tumor Visualization through MRI Off-On Switching of NaGdF<sub>4</sub>-CaCO<sub>3</sub> Nanoconjugates. *Adv. Mater.* **2019**, *31*, 1901851.
- (16) Zhao, Z.; Fan, H.; Zhou, G.; Bai, H.; Liang, H.; Wang, R.; Zhang, X.; Tan, W. Activatable Fluorescence/MRI Bimodal Platform for Tumor Cell Imaging via MnO<sub>2</sub> Nanosheet-Aptamer Nanoprobe. *J. Am. Chem. Soc.* **2014**, *136*, 11220–11223.
- (17) Li, F.; Liang, Z.; Liu, J.; Sun, J.; Hu, X.; Zhao, M.; Liu, J.; Bai, R.; Kim, D.; Sun, X.; Hyeon, T.; Ling, D. Dynamically Reversible Iron Oxide Nanoparticle Assemblies for Targeted Amplification of T<sub>1</sub>-Weighted Magnetic Resonance Imaging of Tumors. *Nano Lett.* **2019**, *19*, 4213–4220.
- (18) Ling, D.; Park, W.; Park, S. J.; Lu, Y.; Kim, K. S.; Hackett, M. J.; Kim, B. H.; Yim, H.; Jeon, Y. S.; Na, K.; Hyeon, T. Multifunctional Tumor pH-Sensitive Self-Assembled Nanoparticles for Bimodal Imaging and Treatment of Resistant Heterogeneous Tumors. *J. Am. Chem. Soc.* **2014**, *136*, 5647–5655.
- (19) Zhang, Z.; Hossain, M. F.; Takahashi, T. Self-Assembled Hematite ( $\alpha$ -Fe<sub>2</sub>O<sub>3</sub>) Nanotube Arrays for Photoelectrocatalytic Degradation of Azo Dye under Simulated Solar Light Irradiation. *Appl. Catal., B* **2010**, *95*, 423–429.
- (20) Muruganandham, M.; Amutha, R.; Ahmmad, B.; Repo, E.; Sillanpää, M. Self-Assembled Fabrication of Superparamagnetic Highly Stable Mesoporous Amorphous Iron Oxides. *J. Phys. Chem. C* **2010**, *114*, 22493–22501.
- (21) Xiang, X.; Wang, Z.; Shi, X.; Fan, M.; Sun, X. Ammonia Synthesis from Electrocatalytic N<sub>2</sub> Reduction under Ambient Conditions by Fe<sub>2</sub>O<sub>3</sub> Nanorods. *ChemCatChem* **2018**, *10*, 4530–4535.
- (22) Grosvenor, A. P.; Kobe, B. A.; Biesinger, M. C.; McIntyre, N. S. Investigation of Multiplet Splitting of Fe 2p XPS Spectra and Bonding in Iron Compounds. *Surf. Interface Anal.* **2004**, *36*, 1564–1574.
- (23) Husain, H.; Hariyanto, B.; Sulthanol, M.; Thamatteng, P.; Pratapa, S. Local Structure Examination of Mineral-Derived Fe<sub>2</sub>O<sub>3</sub> Powder by Fe K-Edge EXAFS and XANES. *IOP Conf. Ser.: Mater. Sci. Eng.* **2018**, *367*, 012027.
- (24) Moscoso-Londoño, O.; Carrião, M. S.; Cosío-Castañeda, C.; Bilovol, V.; Sánchez, R. M.; Lede, E. J.; Socolovsky, L. M.; Martínez-



García, R. One-Step Room Temperature Synthesis of Very Small  $\gamma$ - $\text{Fe}_2\text{O}_3$  Nanoparticles. *Mater. Res. Bull.* **2013**, *48*, 3474–3478.

(25) Jiao, F.; Harrison, A.; Jumas, J. C.; Chadwick, A. V.; Kockelmann, W.; Bruce, P. G. Ordered Mesoporous  $\text{Fe}_2\text{O}_3$  with Crystalline Walls. *J. Am. Chem. Soc.* **2006**, *128*, 5468–5474.

(26) Decker, S.; Lagadic, I.; Klabunde, K. J.; Moscovici, J.; Michalowicz, A. EXAFS Observation of the Sr and Fe Site Structural Environment in SrO and  $\text{Fe}_2\text{O}_3$ -Coated SrO Nanoparticles Used as Carbon Tetrachloride Destructive Adsorbents. *Chem. Mater.* **1998**, *10*, 674–678.

(27) Martínez-Esaín, J.; Faraudo, J.; Puig, T.; Obradors, X.; Ros, J.; Ricart, S.; Yáñez, R. Tunable Self-Assembly of  $\text{YF}_3$  Nanoparticles by Citrate Mediated Ionic Bridges. *J. Am. Chem. Soc.* **2018**, *140*, 2127–2134.

(28) Li, B.; Gu, Z.; Kurniawan, N.; Chen, W.; Xu, Z. Manganese-Based Layered Double Hydroxide Nanoparticles as a  $T_1$ -MRI Contrast Agent with Ultrasensitive pH Response and High Relaxivity. *Adv. Mater.* **2017**, *29*, 1700373–1700373.

(29) Ju, S.; Teng, G.; Zhang, Y.; Ma, M.; Chen, F.; Ni, Y. *In Vitro* Labeling and MRI of Mesenchymal Stem Cells from Human Umbilical Cord Blood. *Magn. Reson. Imaging* **2006**, *24*, 611–617.

(30) Babič, M.; Horák, D.; Trchová, M.; Jendelová, P.; Glogarová, K.; Lesný, P.; Herynek, V.; Hájek, M.; Syková, E. Poly(l-lysine)-Modified Iron Oxide Nanoparticles for Stem Cell Labeling. *Bioconjugate Chem.* **2008**, *19*, 740–750.

(31) Horák, D.; Babič, M.; Jendelová, P.; Herynek, V.; Trchová, M.; Likavčanová, K.; Kapcalová, M.; Hájek, M.; Syková, E. Effect of Different Magnetic Nanoparticle Coatings on the Efficiency of Stem Cell Labeling. *J. Magn. Magn. Mater.* **2009**, *321*, 1539–1547.

(32) Song, G.; Hao, J.; Liang, C.; Liu, T.; Gao, M.; Cheng, L.; Hu, J.; Liu, Z. Degradable Molybdenum Oxide Nanosheets with Rapid Clearance and Efficient Tumor Homing Capabilities as a Therapeutic Nanoplatfrom. *Angew. Chem., Int. Ed.* **2016**, *55*, 2122–2126.

(33) Du, B.; Yu, M.; Zheng, J. Transport and Interactions of Nanoparticles in the Kidneys. *Nat. Rev. Mater.* **2018**, *3*, 358–374.

(34) Liu, J.; Yu, M.; Zhou, C.; Zheng, J. Renal Clearable Inorganic Nanoparticles: A New Frontier of Bionanotechnology. *Mater. Today* **2013**, *16*, 477–486.

(35) Xu, J.; Yu, M.; Peng, C.; Carter, P.; Tian, J.; Ning, X.; Zhou, Q.; Tu, Q.; Zhang, G.; Dao, A.; Jiang, X.; Kapur, P.; Hsieh, J.-T.; Zhao, X.; Liu, P.; Zheng, J. Dose Dependencies and Biocompatibility of Renal Clearable Gold Nanoparticles: From Mice to Non-Human Primates. *Angew. Chem., Int. Ed.* **2018**, *57*, 266–271.

(36) Mukhopadhyay, P.; Chakraborty, S.; Bhattacharya, S.; Mishra, R.; Kundu, P. P. pH-Sensitive Chitosan/Alginate Core-Shell Nanoparticles for Efficient and Safe Oral Insulin Delivery. *Int. J. Biol. Macromol.* **2015**, *72*, 640–648.

(37) Jasim, D. A.; Murphy, S.; Newman, L.; Mironov, A.; Prestat, E.; McCaffrey, J.; Menard-Moyon, C.; Rodrigues, A. F.; Bianco, A.; Haigh, S.; Lennon, R.; Kostarelos, K. The Effects of Extensive Glomerular Filtration of Thin Graphene Oxide Sheets on Kidney Physiology. *ACS Nano* **2016**, *10*, 10753–10767.

(38) Mazue, G.; Newman, A. J.; Scampini, G.; Torre, P. D.; Hard, G. C.; Iatropoulos, M. J.; Williams, G. M.; Bagnasco, S. M. The Histopathology of Kidney Changes in Rats and Monkeys following Intravenous Administration of Massive Doses of FCE 26184, Human Basic Fibroblast Growth Factor. *Toxicol. Pathol.* **1993**, *21*, 490–501.